arXiv:1410.8134v1 [astro-ph.SR] 29 Oct 2014

The VLA Nascent Disk And Multiplicity (VANDAM) Survey of Perseus Protostars. Resolving the Sub-Arcsecond Binary System in NGC 1333 IRAS2A

John J. Tobin[1,13,14], Michael M. Dunham[2], Leslie W. Looney[3], Zhi-Yun Li[4], Claire J. Chandler[5], Dominique Segura-Cox[3], Sarah I. Sadavoy[6], Carl Melis[7], Robert J. Harris[3], Laura M. Perez[5,15], Kaitlin Kratter[8], Jes. K. Jørgensen[9,10], Adele L. Plunkett[11], Charles L. H. Hull[12]

ABSTRACT

We are conducting a Jansky VLA Ka-band (8 mm and 1 cm) and C-band (4 cm and 6.4 cm) survey of all known protostars in the Perseus Molecular Cloud, providing resolution down to $\sim$0.″06 and $\sim$0.″35 in Ka-band and C-band, respectively. Here we present first results from this survey that enable us to examine the source NGC 1333 IRAS2A in unprecedented detail and resolve it into a proto-binary system separated by 0.″621$\pm$0.″006 ($\sim$143 AU) at 8 mm, 1 cm, and 4 cm. These 2 sources (IRAS2A VLA1 and VLA2) are likely driving the two orthogonal outflows known to originate from IRAS2A. The brighter source IRAS2A VLA1 is extended perpendicular to its outflow in the VLA data, with a deconvolved size of 0.″055 ($\sim$13 AU), possibly tracing a protostellar disk. The recently reported candidate companions (IRAS2A MM2 and MM3) are not detected in either our VLA data, CARMA 1.3 mm data, or SMA 850

[1]National Radio Astronomy Observatory, Charlottesville, VA 22903

[2]Harvard-Smithsonian Center for Astrophysics, Cambridge, MA 02138

[3]Department of Astronomy, University of Illinois, Urbana, IL 61801

[4]Department of Astronomy, University of Virginia, Charlottesville, VA 22903

[5]National Radio Astronomy Observatory, Socorro, NM 87801

[6]Max-Planck-Institut für Astronomie, D-69117 Heidelberg, Germany

[7]Center for Astrophysics and Space Sciences, University of California, San Diego, CA 92093

[8]University of Arizona, Steward Observatory, Tucson, AZ 85721

[9]Niels Bohr Institute, University of Copenhagen, Juliane Maries Vej 30, DK-2100 Copenhagen Ø., Denmark

[10]Centre for Star and Planet Formation & Natural History Museum of Denmark, University of Copenhagen, Øster Voldgade 5–7, DK-1350 Copenhagen K., Denmark

[11]Department of Astronomy, Yale University, New Haven CT 06520

[12]Astronomy Department & Radio Astronomy Laboratory, University of California, Berkeley, CA 94720

[13]Current Address: Leiden Observatory, Leiden University, PO Box 9513, 2300 RA, Leiden, The Netherlands; tobin@strw.leidenuniv.nl

[14]Hubble Fellow

[15]Jansky Fellow of the National Radio Astronomy Observatory

μm data. SMA CO ($J = 3 \rightarrow 2$), CARMA CO ($J = 2 \rightarrow 1$), and lower resolution CARMA CO ($J = 1 \rightarrow 0$) observations are used to examine the outflow origins and the nature of the candidate companions to IRAS2A VLA1. The CO ($J = 3 \rightarrow 2$) and ($J = 2 \rightarrow 1$) data show that IRAS2A MM2 is coincident with a bright CO emission spot in the east-west outflow, and IRAS2A MM3 is within the north-south outflow. In contrast, IRAS2A VLA2 lies at the east-west outflow symmetry point. We propose that IRAS2A VLA2 is the driving source of the East-West outflow and a true companion to IRAS2A VLA1, whereas IRAS2A MM2 and MM3 may not be protostellar.

Subject headings: ISM: individual (NGC 1333) — planetary systems: proto-planetary disks — stars: formation

1. Introduction

The formation of binary and multiple star systems is a common outcome of the star formation process. The multiplicity frequency of field stars is a strong function of spectral type, with higher fractions of multiple systems in early-type stars compared to late-type stars. For example, nearly all O stars, about half of all solar-type stars, and about 35% of M stars are multiples, with multiplicity declining into the brown dwarf regime (Sana & Evans 2011; Raghavan et al. 2010; Lada 2006; Duchêne & Kraus 2013). The even higher multiplicity fractions observed in young star forming regions like Taurus suggest that binary formation is commensurate with star formation (Kraus et al. 2011).

Many studies have sought to characterize multiplicity during the protostellar phase of the star formation process. The youngest identifiable protostars are the Class 0 sources, characterized by a dense envelope of gas and dust surrounding the central object (Andre et al. 1993). Class I protostellar systems are more-evolved, having envelopes that are substantially less optically thick and have a smaller reservoir of mass. The formation of a circumstellar disk also takes place in the Class 0 and I phases due to conservation of angular momentum during collapse (Cassen & Moosman 1981). Finally, there are also Class II sources, pre-main sequence stars with an infrared excess above the stellar photosphere indicative of a proto-planetary disk, and Class III without an infrared excess. (Lada 1987).

Looney et al. (2000) conducted one of the first large censuses of multiplicity toward Class 0 protostars, finding a high incidence of multiplicity toward Class 0 protostars on $\sim$1000 AU scales. Similarly, Connelley et al. (2008) found that the more-evolved Class I protostars also have a high degree of multiplicity, in excess of the field stars. A more recent high-resolution study of 5 Class 0 protostars by Maury et al. (2010) did not detect any binary sources between 150 AU and 550 AU; these results combined with those of Looney et al. (2000) and Connelley et al. (2008) lead the authors to suggest that multiplicity increased from the Class 0 to Class I phase. On the other hand, a larger Class 0 sample examined by Chen et al. (2013) found the opposite trend, that

multiplicity is highest in the Class 0 phase and decreases with evolution (see PPVI review Reipurth et al. 2014). Despite recent progress, the Chen et al. (2013) sample was limited by non-uniform resolution, non-uniform sensitivity, and a large mean linear resolution of 600 AU, which is much larger than the median field star separation of ∼50 AU. These limitations make inferences on the origin of multiplicity difficult from the current data.

The dominant modes of multiple system formation are (1) the fragmentation of the core or envelope during collapse due to turbulence and/or rotation in the envelope (e.g., Inutsuka & Miyama 1992; Burkert & Bodenheimer 1993; Offner et al. 2010; Boss & Keiser 2013, 2014) and (2) the fragmentation of a rotationally supported accretion disk via gravitational instability (e.g., Bonnell & Bate 1994a,b; Kratter et al. 2010; Vorobyov & Basu 2010). Disk fragmentation will preferentially form relatively close binaries, while turbulent/rotational fragmentation can form relatively wide multiples that may (or may not) evolve to smaller separations. Both routes point to formation early in the star formation process when there is still a significant mass reservoir available. Since Class 0 sources have large massive envelopes that obscure most radiation shortward of 10 μm, high resolution millimeter/centimeter imaging is needed to reveal multiple systems.

To characterize the multiplicity of protostellar systems in a systematic manner, we are using the Karl G. Jansky Very Large Array (VLA) to conduct the VLA Nascent Disk and Multiplicity survey (VANDAM) toward all known protostars in the Perseus molecular cloud. Perseus is one of the nearest star forming regions at a distance of ∼230 pc (Hirota et al. 2008, 2011). This survey is being conducted at four wavelengths: 8 mm/1 cm (Ka-band) and 4 cm/6.6 cm (C-band). The best resolution of the survey is $\sim 0\farcs06$ (14 AU) in Ka-band, with observations in both A and B configurations. The C-band data were taken in only A configuration, yielding $\sim 0\farcs35$ (80 AU) resolution. The Ka-band observations toward protostars are typically sensitive to a combination of thermal dust emission and thermal free-free emission from protostellar jets, and the C-band data are sensitive to thermal free-free emission and non-thermal synchrotron emission (if present) (Anglada 1995). We observed all the reported protostars in the Enoch et al. (2009) *Spitzer Space Telescope* survey in addition to millimeter-detected sources (Enoch et al. 2010; Chen et al. 2010; Pineda et al. 2011; Schnee et al. 2012; Hirano et al. 1999) and some far infrared sources detected by the *Herschel Space Observatory* Gould Belt Survey of Perseus (e.g., Pezzuto et al. 2012; Sadavoy et al. 2014).

Many of the best studied and most luminous protostars are located in the NGC 1333 sub-region of Perseus. NGC 1333 IRAS2A (hereafter IRAS2A), in particular, has received intensive study of its multiplicity (Looney et al. 2000; Maury et al. 2010), outflows (Sandell et al. 1994; Engargiola & Plambeck 1999; Sandell & Knee 2001; Wakelam et al. 2005; Plunkett et al. 2013; Codella et al. 2014a; Walker-Smith et al. 2014), chemistry (Jørgensen et al. 2004a, 2005; Maury et al. 2014), and kinematics (Brinch et al. 2009; Maret et al. 2014). Sandell et al. (1994) found two nearly orthogonal bi-polar outflows apparently originating from IRAS2A in a single-dish CO map, and Engargiola & Plambeck (1999) more clearly resolved the outflows with a BIMA CO ($J = 1 \rightarrow 0$) map of the region. The two outflows have long been regarded as evidence for a close multiple (Jørgensen

et al. 2004b) given the similarities to other multiple outflow proto-binaries (e.g., L723, Carrasco-González et al. 2008; Girart et al. 2009). While several high-resolution studies failed to identify a close companion (Looney et al. 2000; Maury et al. 2010), recent Plateau de Bure Interferometer (PdBI) observations of IRAS2A detected the main protostellar source and two candidate companion sources in maps of 1.4 mm dust continuum emission, denoted MM1, MM2, and MM3 (Maury et al. 2014; Codella et al. 2014a). MM1 is the brightest source and the candidate companions to MM1 are separated by $2\farcs4$ (MM2) and $2\farcs5$ (MM3), respectively. Although both MM2 and MM3 were detected at 1.4 mm, only MM2 was also detected at 3.2 mm. Thus, Codella et al. (2014a) considered MM2 as protostellar and MM3 as a possible outflow feature.

In this paper, we present new VLA Ka-band and C-band continuum observations toward IRAS2A, with unprecedented angular resolution and sensitivity. We detect a new component separated from the main source by $< 1''$ in our VLA data at 8 mm, 1 cm, and 4 cm. In contrast, neither MM2 nor MM3 are detected in our VLA data or complementary 1.3 mm and 850 μm imaging. We describe the observations in Section 2, the continuum imaging results are discussed in Section 3, the flux densities and spectral indices in Section 4, and discuss the sources in the context of the outflows in Section 5. The results are discussed in Section 6, and our conclusions are summarized in Section 7.

2. Observations

2.1. VLA Observations

We observed IRAS2A with the VLA in Ka-band in B and A configuration on 2013 November 04 and 2014 February 21, respectively. The Ka-band observations were taken in 3-bit mode, providing 8 GHz of bandwidth that are divided into 64 sub-bands, each with 128 MHz bandwidth and 2 MHz channels and full polarization products. We centered one 4 GHz baseband at 36.9 GHz and the other at 28.5 GHz. IRAS2A was observed in B configuration within two 3.5 hour scheduling blocks (one pre-transit and one post-transit), sharing a track with two other sources. The A configuration data were obtained in a 3 hour scheduling block shared with only one other source. 3C48 and 3C84 were observed as the absolute flux and bandpass calibrators, respectively. The science observations were conducted in fast-switching mode to compensate for the rapid atmospheric phase variations, alternating between the science target and gain calibrator (J0336+3218) with a total cycle time of 2.5 minutes; pointing solutions were updated once every 50 minutes. The total time on source was $\sim$60 minutes in B-configuration and $\sim$35 minutes in A-configuration.

The C-band data were taken on 16 March 2014 in 8-bit mode, yielding 2 GHz of bandwidth divided into sixteen 128 MHz sub-bands with 2 MHz channels and full polarization. We centered one baseband at 4.7 GHz and the other at 7.3 GHz. This setup avoids RFI between 4.0 GHz and 4.2 GHz and sensitivity degradation near the band edges. The scheduling block was 3 hours long and shared observations with another field. We observed 3C48 as both the absolute flux density

and bandpass calibrator for 10 minutes, then the gain calibrator, J0336+3218, for 1 minute and the science fields for 9 minutes. The total time on source for each science field was ∼60 minutes. Pointing updates were not necessary at C-band due to the large primary beam.

The data were reduced using CASA 4.1.0 and version 1.2.2 of the VLA pipeline. Flags applied include sub-band edges and the online flags generated by the VLA system. We carried out additional data editing by examining the gain, phase, and bandpass calibration solutions. We flagged the calibration solutions that did not follow expected trends and then applied these flags to the calibrated measurement set using the *applycal* task in *flagonly* mode, which flags the science data without accompanying or flagged calibration solutions. The data were imaged using the *clean* task in multi-frequency synthesis mode with a mask drawn close to the source emission in the dirty map down to a level twice the rms noise. When imaging the full bandwidth of the two widely separated basebands in Ka-band and C-band we used the nterms = 2 option for *clean*. With this option, the sky brightness is modeled as a linear combination of Gaussian-like functions with amplitudes defined by Taylor-polynomials as a function of frequency. For imaging of the individual basebands (4 GHz for Ka-band and 1 GHz for C-band) we only used nterms = 1 due to the lower fractional bandwidth. Imaging was performed iteratively, cleaning and rechecking the image for new sources apparent after cleaning the brightest sources; this step was especially important for the C-band data which had numerous extragalactic sources dominating the dirty maps. The absolute flux calibration uncertainty of the VLA datasets is ∼10%.

2.2. CARMA Observations

We observed IRAS2A with the Combined Array for Research in Millimeter-wave Astronomy (CARMA), located in the Inyo Mountains of California in B and C array configurations. The C-array data were taken on 2013 October 20 and 21, and the B-array data were taken on 2013 December 17. The B-array data were taken during a move to a more compact configuration with only with 8 antennas operating (6 - 10.4 m and 2 - 6.1 m). The central frequency was 225 GHz, the correlator was configured for single polarization, and all 8 windows were configured for 500 MHz continuum with 15 channels each. The flux calibrator was MWC349, and 3C84 was both the bandpass and gain calibrator. The C-array data were taken in dual-polarization mode with a single 500 MHz continuum window and the other three windows configured for spectral line observations; in dual-polarization mode the total number of independent spectral windows is halved. The spectral lines observed were ^{12}CO, ^{13}CO, and C^{18}O ($J = 2 \rightarrow 1$), but only the ^{12}CO data are discussed in this paper. The C-array data observed Uranus as the flux calibrator and 3C84 as both the bandpass and gain calibrator. The data were edited, calibrated, and imaged using the Multichannel Image Reconstruction, Image Analysis, and Display (MIRIAD) software package (Sault et al. 1995); see Tobin et al. (2013) for further details on CARMA data reduction. The absolute flux calibration uncertainty of the CARMA datasets is ∼10% - 20%.

We also utilized subsets of two archival CARMA D and E-array datasets in this study: 1.3

mm continuum and CO ($J = 2 \rightarrow 1$) data obtained as part of the TADPOL project and described in Hull et al. (2014) and 3 mm CO ($J = 1 \rightarrow 0$) data presented by Plunkett et al. (2013). The observations and data reduction are discussed in the relevant publications.

2.3. SMA Observations

Observations of IRAS2A in CO ($J = 3 \rightarrow 2$) line emission and 850 μm continuum were obtained with the Submillimeter Array (SMA, Ho et al. 2004) in both the compact and extended configurations on 2004 October 17 and 2006 January 08, respectively, providing projected baselines ranging from approximately $5 - 220$ m. These data were previously published in Jørgensen et al. (2005) and Brinch et al. (2009) for the compact and extended configurations, respectively. The correlator was configured to provide 256 channels in the 104 MHz band, providing a channel separation and total bandwidth of 0.35 km s^{-1} and 90 km s^{-1}, respectively. Bright, nearby quasars were used for bandpass and gain calibration following standard calibration procedures, and the absolute flux calibration is accurate to $\sim$20%. The data were inspected, flagged, and calibrated using the MIR software package[1] and imaged, cleaned, and restored using the MIRIAD software package configured for the SMA[2].

3. Continuum Imaging Results

The continuum emission from IRAS2A is detected at both Ka-band and C-band. Figure 1 shows the detection emission toward IRAS2A for Ka-band (9 mm) and C-band (4 cm and 6.4 cm) from the A-configuration observations or the combined A and B configuration data. Additionally, Figure 1 also includes a zoom-in of the 9 mm image using only A-configuration data. Both 9 mm images show a clear detection of a secondary source separated by $0\farcs621 \pm 0\farcs006$ ($\sim$143 AU), and this secondary source is detected with a signal-to-noise ratio (SNR) of 41 (A+B combined image); see Table 1. We designate the brighter source as IRAS2A VLA1 (hereafter VLA1) and the new, fainter source as IRAS2A VLA2 (hereafter VLA2). The positions of VLA1 and VLA2 are 03:28:55.5695, +31:14:37.020 and 03:28:55.563, +31:14:36.41, respectively, and are derived from Gaussian fits to the A+B combined 9 mm image shown in Figure 1. The 4 cm image also shows the two sources, though the secondary source is only detected with SNR $\sim$5 and it is located within 1/4 beam of the Ka-band position. VLA1 is detected at 6.4 cm, but VLA2 is undetected at 6.4 cm. The non-detection of VLA2 at 6.4 cm is consistent with a declining spectral index (see Section 4).

The 9 mm images show extended structure in the vicinity of VLA1. The A+B combined image shows some faint diffuse emission extending northwest of VLA1, and the A-array image shows that

[1]Available at https://www.cfa.harvard.edu/$\sim$cqi/mircook.html

[2]Available at http://www.cfa.harvard.edu/sma/miriad/

the source appears extended perpendicular to its outflow direction (see Section 5 for discussion of the outflows). Gaussian fits to the 9 mm image of VLA1 yields a deconvolved position angle of 111.6°, nearly perpendicular to the outflow (see Table 1); the 8 mm and 1 cm images alone also have consistent position angles. Thus, in addition to resolving a close companion source (VLA2), we are also resolving compact structure toward VLA1. VLA2 does not appear to have significant resolved structure with our current resolution.

The main continuum source, VLA1, is spatially coincident with the brightest millimeter source MM1 as identified by Codella et al. (2014a). The secondary sources detected by these authors (MM2 and MM3), however, are not detected in either Ka-band or C-band. Codella et al. (2014a) measured MM2 to have a peak 1.4 mm intensity of 15 mJy/beam and to be unresolved; they also claim a detection at 3.2 mm of 2 mJy/beam giving a spectral index (α) of 2 to 2.5 (we will use the convention of $S_\lambda \propto \lambda^{-\alpha}$ throughout this paper). However, their 3.2 mm map suggests that this 3.2 mm detection is tentative. Extrapolating the MM2 flux densities to 8 mm with $\alpha = 2.0$ (2.5), the expected peak intensity is 0.46 (0.19) mJy/beam (assuming unresolved emission). The rms noise of our Ka-band image is 8.4 μJy/beam, thus, MM2 should be detected with SNR = 55 (22.5) for α = 2.0 (2.5). MM3 has a peak 1.4 mm intensity of 21 mJy/beam and was not detected at 3.2 mm, indicating a $\alpha \gtrsim 4$. This source would fall below our sensitivity, but Codella et al. (2014a) did not claim a protostellar origin for this source, despite it being brighter than MM2.

Our non-detections with the VLA are not necessarily surprising, given that Maury et al. (2010) did not detect MM2 or MM3 at 1.3 mm in observations of IRAS2A with higher spatial resolution and comparable sensitivity (σ=1.16 mJy/beam). Furthermore, Chen et al. (2013) did not detect MM2 or MM3 in 850 μm SMA data despite having sufficient resolution and sensitivity. The lack of detection in our VLA data combined with these facts prompted us to further investigate the nature of MM2 and MM3.

The left panel of Figure 2 shows a 1.3 mm CARMA continuum image of IRAS2A consisting of data from B, C, and D-arrays with tapering and robust weighting applied. No point-like emission is observed toward MM2 or MM3 despite having sufficient sensitivity to detect them at a level better than 8σ, although the 1.3 mm emission is extended toward their locations. We show a higher resolution 1.3 mm image in Figure 2 that is still sensitive enough to detect MM2 and MM3 at better than 10σ. These data also have sufficient resolution to resolve VLA2 and there is emission at the position of VLA2 at the 5σ level, slightly extended from VLA1. We caution that this is a very tentative detection of VLA2 at 1.3 mm, and higher sensitivity imaging is necessary to clearly resolve and detect VLA2 at millimeter wavelengths.

SMA 850 μm images of IRAS2A are shown in Figure 3; these images are derived from the same data presented by Chen et al. (2013, Figure 5). Like the CARMA 1.3 mm data, no point-like

[2]The lower-resolution has less sensitivity because it does not completely recover the extended envelope emission, leading to imaging artifacts with larger amplitudes than at higher resolution

emission toward the locations of MM2 and MM3 is detected. MM2 and MM3 have expected peak flux densities at 850 μm of 40.3 mJy beam^{-1} and 72 mJy beam^{-1} respectively, assuming $\alpha = 2.0$. In the highest-resolution image, we do detect extended emission at the location of MM2 with a peak intensity of $\sim$ 15 mJy/beam, but this is much fainter than expected from the observations of Codella et al. (2014a). We also note that Chen et al. (2013) suggested a different companion source, and we do not find evidence for this source in our VLA or CARMA data.

4. Flux Densities and Spectral Indices

The flux densities of IRAS2A VLA1 and VLA2 were measured using Gaussian fits to the images at each wavelength from 850 μm to 6.4 cm using the CASA task *imfit* (see Table 1). The Gaussian fits were performed simultaneously for the two sources at wavelengths between 1.3 mm and 4 cm; single source fits were conducted for 850 μm and 6.4 cm. For the 1.3 mm fit to VLA2, it was also necessary to fix the source position and assume that it is unresolved. We also included the 2.7 mm continuum flux from Looney et al. (2000) to better constrain the thermal dust slopes; VLA1 was detected in these data and an upper limit is provided for VLA2. We have used these data to plot the radio spectra of these sources in Figure 4, where the Ka-band flux densities are taken from the A+B combined imaging. The broad wavelength coverage is dominated by thermal dust emission at the short wavelength end and free-free continuum at the long-wavelength end. We have attempted to decompose the radio spectra into their free-free and thermal dust components, assuming that the emission spectrum of both can be described by power-laws.

We used the *mpfit* routines (Markwardt 2009) to perform a two-component linear fit to the data. In addition to the statistical uncertainty, we adopt an additional 25% uncertainty at 1.3 mm and 850 μm, 10% uncertainty at 8 mm, 9 mm, and 1.03 cm, and 5% uncertainty at 4 cm, 4.9 cm, and 6.4 cm. Larger uncertainties are assumed at the shorter wavelengths because of greater calibration uncertainty and sensitivity to dust emission from larger scales than probed by the VLA. The 850 μm data will also include flux from both sources, but VLA2 is apparently much fainter than VLA1 at shorter wavelengths.

For VLA1, where we had the most available data, we first simultaneously fit the data using a two-component linear fit (method 1; described above). We also fitted the slopes in a two step process where we used the 4 cm and 6.4 cm data alone to derive a spectral slope of the free-free emission (method 2; implicitly assumes no dust is contributing at those wavelengths). We then used the free-free slope as a fixed parameter and fit the slope of the thermal dust emission. The result from the two-step process is shown in Figure 4. We note that both methods yield consistent slopes within the uncertainties (see Table 2). The simultaneous fits yield shallower slopes for both the thermal dust and free-free emission than the two-step fits. We adopt the free-free spectral index of 1.1 from the 4 cm to 6.4 cm fit (method 2) as the most reliable. Thus, the relative contributions of thermal dust emission to the continuum emission at 8 mm, 9 mm, and 1.03 cm are 53%, 43%, and 29% respectively.

The spectral indices of VLA2 were more difficult to derive accurately for both the dust and free-free components due to weaker emission and non-detections at both the shortest and longest wavelengths. We were only able to perform a simultaneous fit of the thermal and free-free components because the source was not detected at 6.4 cm. The thermal slope is poorly constrained, and the source appears to be dominated by free-free emission at $\lambda \gtrsim 2$ mm. To better constrain the free-free slope, we assumed a thermal component with a fixed spectral index of -3.0 (this is similar to that of VLA1 and implies a dust opacity spectral index of 1 in the optically thin limit), comparable to previous observations of young stellar objects (Rodmann et al. 2006; Melis et al. 2011; Tobin et al. 2013). We also fit a single slope to all the VLA data ($\lambda > 7$ mm), and we find a slope equivalent to the free-free slope derived from the fit with a fixed thermal dust power-law. In both cases, the free-free emission is $> 50\%$ of the total continuum flux to $\lambda \sim 1$ mm.

The cm-wave spectral indices (α) are 1.1 ± 0.19 and 1.7 ± 0.15 for VLA1 and VLA2, respectively. These spectral indices are consistent with previous observations of free-free emission toward protostellar objects, with moderately optically thick emission (Anglada et al. 1998; Shirley et al. 2007). The spectral indices for VLA1 and VLA2 indicate optical depths of $\sim$0.9 and $\sim$2 at 4 cm, respectively (Anglada et al. 1998, Equation 6). Note that our flux densities at 4 cm for VLA1 differ by a factor of $\sim$2 from the values at 3.6 cm (0.22 mJy) given in Rodríguez et al. (1999) and Reipurth et al. (2002); however, the 6 cm flux density in Rodríguez et al. (1999) is consistent with our 6.4 cm measurement. Spatial filtering is not likely the cause of the discrepancy at 4 cm because Reipurth et al. (2002) also observed VLA1 in A-configuration and VLA2 is too faint to cause the difference. Thus, the source may be exhibiting intrinsic variability. Due to the lower flux density at 4 cm, the spectral index we measure at centimeter wavelengths is significantly smaller than the value of 2.6 ± 0.4 found by Rodríguez et al. (1999).

5. Outflow Driving Sources

Sandell et al. (1994) first observed the two orthogonal outflows driven from IRAS2A, but their single-dish maps could not identify the driving sources. Interferometric maps of CO ($J = 1 \rightarrow 0$) emission were observed by Engargiola & Plambeck (1999), suggesting a very close proto-binary driving the two outflows from IRAS2A. Figure 5 shows the large-scale CO ($J = 1 \rightarrow 0$) outflows using the data from Plunkett et al. (2013). These data clearly show the well-collimated east-west outflow and a wider, less-collimated north-south outflow. The 4.5 μm emission from Jørgensen et al. (2006) (grayscale in Figure 5) agrees well with the outflow axes defined from the CO emission for the north-south flow. The east-west flow has some tenuous 4.5 μm emission associated with the blue-shifted lobe. We adopt a position angle (PA) of 281° for the east-west outflow and a PA of 201° for the north-south outflow, using the convention of the PA being the angle of the blue-shifted lobe east of north. The PA of each outflow is defined by drawing vectors that align as closely as possible to the CO ($J = 2 \rightarrow 1$) and CO ($J = 3 \rightarrow 2$) emission maps shown in Figure 6.

The smaller-scale outflow emission is highlighted in Figure 6 using higher resolution CO ($J =$

$2 \rightarrow 1$) and CO ($J = 3 \rightarrow 2$) emission. The higher resolution and higher excitation lines show that the north-south outflow becomes well-collimated on smaller scales, and the east-west outflow remains more narrow and well-collimated. VLA1 is clearly located at the base of both the blue-shifted and red-shifted emission from the north-south outflow. Similarly, VLA 2 is located near the origin of the east-west outflow and is in close proximity to the base of the redshifted emission. However, the base of the blue-shifted component is unclear due to blending with the blue-shifted component of the north-south outflow. Imaging only the higher resolution CO ($J = 3 \rightarrow 2$) did not conclusively reveal a blue-shifted lobe near VLA2. In addition to these morphological arguments, it is known that the bolometric luminosity of a protostar is related to the outflow energy (Bontemps et al. 1996; Wu et al. 2004), and the centimeter-wave luminosity (3.6 cm and 6 cm) is also correlated with L_{bol} and the outflow energy (Curiel et al. 1989; Anglada 1995; Shirley et al. 2007). Furthermore, Plunkett et al. (2013) found that the north-south outflow had 6 times more energy than the east-west outflow. These relationships are consistent with VLA1 (brighter at all wavelengths) being the driving source of the north-south outflow and VLA2 driving the less energetic east-west outflow.

The source MM2 from Codella et al. (2014a) is spatially coincident with the peak of the red-shifted CO emission in both maps (see Figure 6). This position is also consistent with the redshifted SiO peak and near the SO peak found by Codella et al. (2014a). The position of MM2 is inconsistent with the origin of the red-shifted east-west outflow, being offset to the east and slightly south of the apparent origin in the CO emission. The non-detection of MM2 in any of our continuum data and placement within the east-west outflow suggests that this source is not likely the driving source of the east-west outflow and that it may not be protostellar in nature. Similarly, MM3 also resides within the blue-shifted north-south outflow from IRAS2A and is located near the peak of CO ($J = 3 \rightarrow 2$) emission, and we agree with Codella et al. (2014a) that it is not likely protostellar.

The placement of VLA1 at the apparent north-south outflow origin coupled with its greater centimeter luminosity indicates that it is most likely the driving source of the north-south outflow. VLA2 is at the base of the red-shifted lobe of the east-west outflow. The lower outflow energy of the east-west outflow and the weaker centimeter luminosity of VLA2 makes this source the most likely candidate to drive the east-west outflow.

6. Discussion

The multiplicity of IRAS2A is important on its own and in the context of the origin of protostellar multiplicity. It is often observed as a prototypical source for envelope structure, infall, tracers, chemistry, and outflow shocks and the multiplicity of this source may have implications for the interpretation of these observations. As we discuss below, the novel high-resolution data presented herein provide evidence for the origin of the IRAS2A system.

The VLA data have enabled us to convincingly resolve IRAS2A into two sources separated by only ∼143 AU. At 8 mm and 1 cm, the dust is expected to be optically thin, and the data are sensitive to a combination of dust and free-free emission, possibly helping sources to stand out even if their dust emission is faint. At 4 cm the continuum should be dominated by free-free emission originating from the base of the protostellar jets (Anglada 1995). IRAS2A VLA2 highlights the utility of probing multiple emission mechanisms, because the CARMA 1.3 mm data with high enough resolution to resolve the binary show only very faint emission toward the position of VLA2. This is an indication that this source has much less circumstellar dust than VLA1. On the other hand VLA2 is quite bright at 8 mm and 1 cm due to free-free emission but still fainter than VLA1. The detection of free-free emission is strong evidence for the presence of a protostellar object because free-free emission is thought to be associated with shocks at the base of the jet, within ∼10 AU of the protostar (Anglada et al. 1998). However, a lack of detected free-free emission is not evidence against a source being protostellar.

Recent PdBI results from Codella et al. (2014a) and Maury et al. (2014) detected two source candidates (MM2 and MM3) within $2\farcs5$ of IRAS2A in dust continuum emission at 1.4 mm. However, we did not detect these sources in our VLA data, despite the estimated flux density of MM2 being within our sensitivity limit at 8 mm. Moreover, any source driving an outflow strong enough to produce shocked emission at its position would naively be expected to have free-free emission associated with it at 4 cm. MM2 and MM3 were also undetected at 1.3 mm and 850 μm. There is 3σ emission at the position of MM2 at 850 μm that appears as part of the structure extending from IRAS2A, and it is below the expected intensity level. Thus, it is clear that caution should be exercised when interpreting continuum maps in which only ∼10% - 20% of the total continuum flux is recovered, and the non-detections of MM2 and MM3 at any wavelength in this study indicates that these sources may be spurious.

Numerous other studies with the PdBI also failed to detect MM2 and MM3, despite having sufficient sensitivity and angular resolution (Coutens et al. 2014; Persson et al. 2012, and Private Communication with those authors). Furthermore, Maury et al. (2010) observed IRAS2A with higher resolution and sensitivity than Codella et al. (2014a) but did not detect either source. Maury et al. (2010) also reported a source $\sim6''$ southeast of IRAS2A (called IRAS2A SE), and we do not detect it in any of our data as well.

The fact that we see emission extended toward the positions of MM2 and MM3 at 850 μm and 1.3 mm suggests that their detections could result from spatial filtering artifacts of extended envelope emission. For example, the uv-plane of the PdBI is sparsely sampled with at most 15 baselines per configuration. Another possibility is that these are outflow-induced continuum features resulting from shock-heating (e.g., Maury et al. 2010), given that they are located near bright CO emission (Figure 4) and at the location of SiO and SO emission (Codella et al. 2014a). However, protostellar outflow shocks are not expected to efficiently heat dust (Draine et al. 1983; Hollenbach & McKee 1989). Nevertheless, if the features did result from outflow shock-heating we would still expect to detect the outflow features at 1.3 mm, 850 μm, and 8 mm since the emission would still

be from dust. It is possible that the VLA could be filtering out this emission, but this emission would not be filtered in the 1.3 mm and 850 μm images that we presented in Figures 2 & 3. Line-contaminated continuum could also explain these sources and their close association with outflow and shock features. Codella et al. (2014a) had sufficient spectral resolution in their continuum bands to identify line-free regions of the continuum, but the spectral line maps shown in Figure 4 of Maury et al. (2014) have point-like emission features that appear coincident with MM2 and MM3 for several molecular lines, notably several methanol and formaldehyde transitions.

In summary, MM2 and MM3 have not been detected in any other continuum dataset available from a multitude of observatories spanning wavelengths shorter and longer than the observations of Codella et al. (2014a). Their association with extended envelope emission in our 1.3 mm and 850 μm continuum data and multiple line emission features in Maury et al. (2014) lead us to conclude that MM2 and MM3 are most likely not protostellar sources. We suggest that the driving source of the north-south outflow is VLA1, and the driving source of the east-west outflow is likely VLA2. Despite the high-resolution of our observations there is still significant blending of the outflow components and higher resolution and higher sensitivity data will be needed to definitively disentangle the outflow driving sources.

6.1. A Compact, Embedded Disk around IRAS2A VLA1?

The continuum emission of IRAS2A VLA is clearly resolved perpendicular to the outflow as shown in Figure 1. Furthermore, Gaussian fits to the data all indicate that the source is resolved and extended perpendicular to the outflow, a possible indication that we have detected a compact disk surrounding VLA1. The deconvolved size of this disk-like structure is quite small, just $0\farcs055$ ($\sim$13 AU) in diameter. Thus, if this is indeed a disk surrounding VLA1, it is about 10 times smaller than the other known Class 0 disks (Tobin et al. 2012; Murillo & Lai 2013; Lindberg et al. 2014; Codella et al. 2014b). We emphasize that if we are detecting the protostellar disk in the Ka-band data, we may not be capturing its full extent. This could be due to surface brightness sensitivity limits and possibly the distribution of dust grain sizes within the disk itself. More-evolved protoplanetary disks are found to be more compact at 8 mm than when viewed at shorter wavelengths due to grain growth and radial drift of dust grains (Pérez et al. 2012), and this process can already be at work in the protostellar phase (Birnstiel et al. 2010). Therefore the actual size of the disk could be larger than the structure we resolve with the VLA. However, the CARMA 1.3 mm data presented in Figure 2 and SMA 850 μm data in Figure 3 do not have indications of a disk $>$ 100 AU in diameter.

The position angle of the disk-like structure is also in nearly the same direction as the velocity gradient observed in methanol emission by Maret et al. (2014). However, the methanol emission was not thought to be associated with the protostellar disk due to its kinematics being inconsistent with Keplerian rotation. Furthermore, the size of the methanol emitting region was $0\farcs44$ (deconvolved), about 8 times larger than the disk-like structure. Brinch et al. (2009) had also investigated the

kinematics of IRAS2A and found no strong evidence of rotation on ∼200 AU scales. Thus, it seems likely that the disk around IRAS2A is smaller than ∼200 AU and perhaps comparable to the size we measure for the disk-like object. Of course, future sub/millimeter observations of both dust continuum and molecular lines at high resolution will be crucial to the further characterization of the disk around this source.

6.2. Origin of IRAS2A System

The mechanism by which binaries form remains a subject of debate. Current theoretical work suggests two dominant mechanisms for the formation of multiple systems: fragmentation on cloud or filament scales (Burkert & Bodenheimer 1993; Bonnell & Bastien 1993; Padoan & Nordlund 2002; Offner et al. 2010) or on disk scales (Bonnell & Bate 1994a; Kratter et al. 2010; Zhu et al. 2012). Fragmentation on core scales is likely due to turbulence (although early work considered rotation), while fragmentation on disk scales is due to gravitational instability. Both disk fragmentation and core fragmentation are likely to contribute to protostellar multiplicity in different environments and for different stellar masses. Because of the small projected separation (∼143 AU), the IRAS2A system naively seems a good candidate for the disk fragmentation scenario. However, the outflows tell a different story. If the outflow from each component of the IRAS2A system is perpendicular to the (inner) disk surrounding each protostar, as expected from the currently favored magneto-centrifugal mechanism for outflow generation (Blandford & Payne 1982; Frank et al. 2014), the disk around the VLA2 should be perpendicular to that of the VLA1. The large relative inclination suggests that the two do not share the same net angular momentum vector, as would be expected if the stars formed in the same protostellar disk.

The turbulent fragmentation model is somewhat more consistent with the data. Turbulent fragmentation typically occurs on larger scales, ∼1000 AU, however separation evolution down to ∼100 AU on timescales of 10^4 yrs is observed in simulations (Offner et al. 2010). If the binary underwent substantial migration, one might expect to see it reflected in changes to the outflow, which we do not observe. The blue-shifted side of the east-west outflow that we associate with VLA2 extends ∼0.1 pc (90″). Assuming a typical outflow velocity between 10 km s^{-1} and 100 km s^{-1} (e.g., Frank et al. 2014) the dynamical age of the outflow could be between 1000 yr and 10000 yr. This calculation assumes that the outflow is exactly in the plane of the sky. Since the outflow is observed closer to edge-on than face-on (Plunkett et al. 2013), the inclination correction would likely be a factor of ∼2. The relatively constant outflow direction over the last 1000 yr to 10000 yr suggests that the orbital migration has been smooth and/or slow enough to preserve the orientation. Such smooth motion rules out dynamical interaction with another body as the means to decrease the separation. The concept of "orbital evolution" for such systems can be somewhat misleading: shrinking separations can occur because the relative velocities are convergent due to global collapse of the birth core or filament. Such evolution will not necessarily cause precession of the star+disk angular momentum vector.

Alternatively, the strong outflow may have only began to be driven after much of the orbital evolution to its current location had finished. A system with a combined mass of 1 $M_{\odot}$ and a semi-major axis of 142 AU would have an orbital period of ∼1,700 yr. If this orbit is highly elliptical, then the bulk of the orbit will be spent at distances far from the dominant component (assumed to be VLA1), and it is possible that the apparent outflow direction would not be appreciably changed. The small 'wiggle' observed in the outflow on scales < 1000 AU could possibly result from movement of VLA2.

Another possibility, albeit unlikely, is that IRAS2A is simply a superposition of two sources along the line of sight, and the true separation is much larger than the projected separation. However, the peak surface density of young stellar objects in NGC 1333 is ∼200 pc^{-2} (Gutermuth et al. 2008), and the probability of two sources being within a projected radius of 143 AU is ∼10^{-4}. Moreover, molecular line observations toward IRAS2A by Volgenau et al. (2006) do not show strong evidence for two cores aligned along the line of sight. The $C^{18}O$, $H^{13}CO^{+}$, and N_2H^{+} spectra have single peaks at resolutions of 10″ and less. Thus, the simplest and most likely possibility is that these two sources are in close physical proximity. High resolution molecular line observations that resolve the two sources are necessary to determine their relative velocities.

We propose that VLA2 most likely formed via turbulent fragmentation. Although misaligned disks are consistent with more-evolved, Class II, binary systems (Jensen & Akeson 2014; Williams et al. 2014), we can only infer the disk misalignment based on outflow directions. Thus, IRAS2A and systems like it could be the predecessors to misaligned proto-planetary disk systems.

6.3. Outflow Emission Structure

The outflow emission from IRAS2A has a few features worth further discussion. The bi-polar east-west outflow that we suggest originates from VLA2 appears quite linear and well-collimated in the CO ($J = 1 \rightarrow 0$) map in Figure 5. However, on smaller-scales the outflow is not quite as symmetric in appearance. The CO emission plots in Figure 6 show a bright lump of red-shifted emission which is consistent with the location of MM2 from Codella et al. (2014a) as well as the locations of the peak SiO and SO emission observed by those authors. However, no equivalent blue-shifted emission was observed on the opposing side of the protostar, in fact there is some low-velocity red-shifted SO on the blue-shifted side of the outflow (Codella et al. 2014a, their Figure 1 and Figure B.2). In the case of the CO emission, the blue-shifted emission near VLA2 could simply be blended with the emission from VLA1. Codella et al. (2014a) suggested that the lack of a strong blue-shifted component near the protostellar source may be due to monopolar jet activity or the jet driving into an inhomogeneous medium where the blue-shifted side is not readily apparent. This statement may hold even for the case of VLA2 being the driving source.

The bright lump of CO emission associated with the position of MM2 and the SiO and SO emission in Codella et al. (2014a) is also slightly offset from the main axis of the larger-scale flow

(see Figure 6). The offset of the red-shifted emission near the protostar, relative to the larger-scale east-west flow, could result from outflow precession, where the more recent ejection events have a slightly different axis than the previous episodes. There is some evidence for blue-shifted emission being offset to the north from the larger-scale east-west flow, but this is offset from the protostar along the outflow by ∼1000 AU. Alternatively, the shift in the outflow could be due to the orbital motion of VLA2 around VLA1. This is plausible because the time required for an outflow of 10 km s^{-1} - 100 km s^{-1} to propagate 1000 AU is ∼ 50 yr - 500 yr, and the orbital period of VLA2 would be ∼1700 yr, assuming VLA1 has a mass of 1 $M_{\odot}$ and the semi-major axis is equal to the current separation. Thus, during the course of outflow propagation VLA2 could have moved through enough of its orbit to exhibit a change in direction. This depends on the combined mass of VLA1 and VLA2 and the orbital parameters.

7. Conclusions

We have presented VLA imaging of the NGC 1333 IRAS2A region at 8 mm, 1 cm, 4 cm, and 6.4 cm with a best resolution of ∼0.″06 (14 AU), resolving two sources toward IRAS2A (VLA1 and VLA2), separated by 0.″621 ± 0.006 (∼143 AU). Emission at 1.3 mm from VLA2 is tentatively detected in complementary CARMA images at the 5σ level. We do not detect the candidate companion sources MM2 and MM3 identified by Codella et al. (2014a) in our VLA data. Moreover, these sources were also not detected in sufficiently sensitive CARMA 1.3 mm data and SMA 850 μm data, as well as other PdBI observations. Extended structure is observed toward the locations of MM2 and MM3 at both 1.3 mm and 850 μm, an indication that these sources could be spatial filtering artifacts or line-contaminated continuum. ^{12}CO ($J = 2 \rightarrow 1$) and ($J = 3 \rightarrow 2$) observations show that MM2 and MM3 are located right in outflow lobes. We conclude that VLA1 is the driving source of the north-south outflow and propose that VLA2 is the driving source of the east-west outflow.

VLA1 is found to be extended perpendicular to the direction of the outflow in the Ka-band imaging. The deconvolved size of the major axis is 0.″055 (∼13 AU). This structure could be part of the protostellar disk around VLA1. In contrast, VLA2 has no evidence of extended structure and is consistent with being a point source.

The spectral indices at centimeter wavelengths for both VLA1 and VLA2 are consistent with moderately to very optically thick free-free emission. The free-free emission from VLA1 accounts for about half the total flux at 8 mm, the other half from thermal dust emission. VLA2, on the other hand, appears dominated by free-free emission until a wavelength of ∼1 mm, indicative of very little circumstellar dust.

The orthogonal outflows from the sources are strong evidence against disk fragmentation being the formation route for the VLA1 and VLA2 binary system. Turbulent fragmentation with orbital evolution is possible and most likely; however, the outflow shows no large-scale changes in direction

over the past 1000 yr - 10000 yr. Future kinematic observations at $\sim 0\farcs25$ resolution have the promise to better characterize the origins of this proto-binary system.

The authors wish to thank the anonymous referee for a constructive report that improve the paper. We also wish to thank L. Kristensen and M. Persson for stimulating discussions regarding this work. J.J.T. acknowledges support provided by NASA through Hubble Fellowship grant #HST-HF-51300.01-A awarded by the Space Telescope Science Institute, which is operated by the Association of Universities for Research in Astronomy, Inc., for NASA, under contract NAS 5-26555. M.M.D. acknowledges support from the Submillimeter Array through an SMA postdoctoral fellowship. L.W.L. acknowledges support from the Laboratory for Astronomical Imaging at the University of Illinois and the NSF under grant AST-07-09206. D.S.-C. acknowledges support provided by the NSF through award GSSP 2013-06713 from the NRAO. C.M. acknowledges financial support from the U.S. National Science Foundation through award AST-1313428. S.I.S. acknowledges support from the National Science and Engineering Research Council of Canada (NSERC) Postdoctoral Fellowship. Z.Y.L. is supported in part by NNX14AB38G and AST-1313083. A.L.P. is supported by the National Science Foundation Graduate Research Fellowship under Grant No. DGE-1122492. L.M.P acknowledges support from the Jansky Fellowship program of the National Radio Astronomy Observatory. Support for CARMA construction was derived from the states of Illinois, California, and Maryland, the James S. McDonnell Foundation, the Gordon and Betty Moore Foundation, the Kenneth T. and Eileen L. Norris Foundation, the University of Chicago, the Associates of the California Institute of Technology, and the National Science Foundation. Ongoing CARMA development and operations are supported by the National Science Foundation under a cooperative agreement, and by the CARMA partner universities. The Submillimeter Array is a joint project between the Smithsonian Astrophysical Observatory and the Academia Sinica Institute of Astronomy and Astrophysics and is funded by the Smithsonian Institution and the Academia Sinica. The National Radio Astronomy Observatory is a facility of the National Science Foundation operated under cooperative agreement by Associated Universities, Inc.

The authors wish to recognize and acknowledge the very significant cultural role and reverence that the summit of Mauna Kea has always had within the indigenous Hawaiian community. We are most fortunate to have the opportunity to conduct observations from this mountain.

Facilities: VLA, CARMA, SMA, *Spitzer*

REFERENCES

Andre, P., Ward-Thompson, D., & Barsony, M. 1993, ApJ, 406, 122

Anglada, G. 1995, in Revista Mexicana de Astronomia y Astrofisica, vol. 27, Vol. 1, Revista Mexicana de Astronomia y Astrofisica Conference Series, ed. S. Lizano & J. M. Torrelles, 67

Anglada, G., Villuendas, E., Estalella, R., et al. 1998, AJ, 116, 2953

Birnstiel, T., Dullemond, C. P., & Brauer, F. 2010, A&A, 513, A79

Blandford, R. D., & Payne, D. G. 1982, MNRAS, 199, 883

Bonnell, I., & Bastien, P. 1993, ApJ, 406, 614

Bonnell, I. A., & Bate, M. R. 1994a, MNRAS, 269, L45

—. 1994b, MNRAS, 271, 999

Bontemps, S., Andre, P., Terebey, S., & Cabrit, S. 1996, A&A, 311, 858

Boss, A. P., & Keiser, S. A. 2013, ApJ, 764, 136

—. 2014, ArXiv e-prints, arXiv:1408.2479

Brinch, C., Jørgensen, J. K., & Hogerheijde, M. R. 2009, A&A, 502, 199

Burkert, A., & Bodenheimer, P. 1993, MNRAS, 264, 798

Carrasco-González, C., Anglada, G., Rodríguez, L. F., et al. 2008, ApJ, 676, 1073

Cassen, P., & Moosman, A. 1981, Icarus, 48, 353

Chen, X., Arce, H. G., Zhang, Q., et al. 2010, ApJ, 715, 1344

—. 2013, ApJ, 768, 110

Codella, C., Maury, A. J., Gueth, F., et al. 2014a, A&A, 563, L3

Codella, C., Cabrit, S., Gueth, F., et al. 2014b, A&A, 568, L5

Connelley, M. S., Reipurth, B., & Tokunaga, A. T. 2008, AJ, 135, 2526

Coutens, A., Jørgensen, J. K., Persson, M. V., et al. 2014, ApJ, 792, L5

Curiel, S., Rodriguez, L. F., Bohigas, J., et al. 1989, Astrophysical Letters and Communications, 27, 299

Draine, B. T., Roberge, W. G., & Dalgarno, A. 1983, ApJ, 264, 485

Duchêne, G., & Kraus, A. 2013, ARA&A, 51, 269

Engargiola, G., & Plambeck, R. L. 1999, in The Physics and Chemistry of the Interstellar Medium, ed. V. Ossenkopf, J. Stutzki, & G. Winnewisser, 291

Enoch, M. L., Evans, N. J., Sargent, A. I., & Glenn, J. 2009, ApJ, 692, 973

Enoch, M. L., Lee, J.-E., Harvey, P., Dunham, M. M., & Schnee, S. 2010, ApJ, 722, L33

Frank, A., Ray, T. P., Cabrit, S., et al. 2014, ArXiv e-prints, arXiv:1402.3553

Girart, J. M., Rao, R., & Estalella, R. 2009, ApJ, 694, 56

Gutermuth, R. A., Myers, P. C., Megeath, S. T., et al. 2008, ApJ, 674, 336

Hirano, N., Kamazaki, T., Mikami, H., Ohashi, N., & Umemoto, T. 1999, in Star Formation 1999, ed. T. Nakamoto, 181–182

Hirota, T., Honma, M., Imai, H., et al. 2011, PASJ, 63, 1

Hirota, T., Bushimata, T., Choi, Y. K., et al. 2008, PASJ, 60, 37

Ho, P. T. P., Moran, J. M., & Lo, K. Y. 2004, ApJ, 616, L1

Hollenbach, D., & McKee, C. F. 1989, ApJ, 342, 306

Hull, C. L. H., Plambeck, R. L., Kwon, W., et al. 2014, ApJS, 213, 13

Inutsuka, S.-I., & Miyama, S. M. 1992, ApJ, 388, 392

Jensen, E. L. N., & Akeson, R. 2014, Nature, 511, 567

Jørgensen, J. K., Bourke, T. L., Myers, P. C., et al. 2005, ApJ, 632, 973

Jørgensen, J. K., Hogerheijde, M. R., Blake, G. A., et al. 2004a, A&A, 415, 1021

Jørgensen, J. K., Hogerheijde, M. R., van Dishoeck, E. F., Blake, G. A., & Schöier, F. L. 2004b, A&A, 413, 993

Jørgensen, J. K., Harvey, P. M., Evans, II, N. J., et al. 2006, ApJ, 645, 1246

Kratter, K. M., Matzner, C. D., Krumholz, M. R., & Klein, R. I. 2010, ApJ, 708, 1585

Kraus, A. L., Ireland, M. J., Martinache, F., & Hillenbrand, L. A. 2011, ApJ, 731, 8

Lada, C. J. 1987, in IAU Symp. 115: Star Forming Regions, ed. M. Peimbert & J. Jugaku, 1–17

Lada, C. J. 2006, ApJ, 640, L63

Lindberg, J. E., Jørgensen, J. K., Brinch, C., et al. 2014, A&A, 566, A74

Looney, L. W., Mundy, L. G., & Welch, W. J. 2000, ApJ, 529, 477

Maret, S., Belloche, A., Maury, A. J., et al. 2014, A&A, 563, L1

Markwardt, C. B. 2009, in Astronomical Society of the Pacific Conference Series, Vol. 411, Astronomical Data Analysis Software and Systems XVIII, ed. D. A. Bohlender, D. Durand, & P. Dowler, 251

Maury, A. J., André, P., Hennebelle, P., et al. 2010, A&A, 512, A40

Maury, A. J., Belloche, A., André, P., et al. 2014, A&A, 563, L2

Melis, C., Duchêne, G., Chomiuk, L., et al. 2011, ApJ, 739, L7

Murillo, N. M., & Lai, S.-P. 2013, ApJ, 764, L15

Offner, S. S. R., Kratter, K. M., Matzner, C. D., Krumholz, M. R., & Klein, R. I. 2010, ApJ, 725, 1485

Padoan, P., & Nordlund, Å. 2002, ApJ, 576, 870

Pérez, L. M., Carpenter, J. M., Chandler, C. J., et al. 2012, ApJ, 760, L17

Persson, M. V., Jørgensen, J. K., & van Dishoeck, E. F. 2012, A&A, 541, A39

Pezzuto, S., Elia, D., Schisano, E., et al. 2012, A&A, 547, A54

Pineda, J. E., Arce, H. G., Schnee, S., et al. 2011, ApJ, 743, 201

Plunkett, A. L., Arce, H. G., Corder, S. A., et al. 2013, ApJ, 774, 22

Raghavan, D., McAlister, H. A., Henry, T. J., et al. 2010, ApJS, 190, 1

Reipurth, B., Clarke, C. J., Boss, A. P., et al. 2014, ArXiv e-prints, arXiv:1403.1907

Reipurth, B., Rodríguez, L. F., Anglada, G., & Bally, J. 2002, AJ, 124, 1045

Rodmann, J., Henning, T., Chandler, C. J., Mundy, L. G., & Wilner, D. J. 2006, A&A, 446, 211

Rodríguez, L. F., Anglada, G., & Curiel, S. 1999, ApJS, 125, 427

Sadavoy, S. I., Di Francesco, J., André, P., et al. 2014, ApJ, 787, L18

Sana, H., & Evans, C. J. 2011, in IAU Symposium, Vol. 272, IAU Symposium, ed. C. Neiner, G. Wade, G. Meynet, & G. Peters, 474–485

Sandell, G., & Knee, L. B. G. 2001, ApJ, 546, L49

Sandell, G., Knee, L. B. G., Aspin, C., Robson, I. E., & Russell, A. P. G. 1994, A&A, 285, L1

Sault, R. J., Teuben, P. J., & Wright, M. C. H. 1995, in Astronomical Society of the Pacific Conference Series, Vol. 77, Astronomical Data Analysis Software and Systems IV, ed. R. A. Shaw, H. E. Payne, & J. J. E. Hayes, 433

Schnee, S., Sadavoy, S., Di Francesco, J., Johnstone, D., & Wei, L. 2012, ApJ, 755, 178

Shirley, Y. L., Claussen, M. J., Bourke, T. L., Young, C. H., & Blake, G. A. 2007, ApJ, 667, 329

Tobin, J. J., Hartmann, L., Chiang, H.-F., et al. 2012, Nature, 492, 83

Tobin, J. J., Bergin, E. A., Hartmann, L., et al. 2013, ApJ, 765, 18

Volgenau, N. H., Mundy, L. G., Looney, L. W., & Welch, W. J. 2006, ApJ, 651, 301

Vorobyov, E. I., & Basu, S. 2010, ApJ, 719, 1896

Wakelam, V., Ceccarelli, C., Castets, A., et al. 2005, A&A, 437, 149

Walker-Smith, S. L., Richer, J. S., Buckle, J. V., Hatchell, J., & Drabek-Maunder, E. 2014, MNRAS, 440, 3568

Williams, J. P., Mann, R. K., Di Francesco, J., et al. 2014, ApJ, arXiv:1410.3570

Wu, Y., Wei, Y., Zhao, M., et al. 2004, A&A, 426, 503

Zhu, Z., Hartmann, L., Nelson, R. P., & Gammie, C. F. 2012, ApJ, 746, 110

This preprint was prepared with the AAS LaTeX macros v5.2.

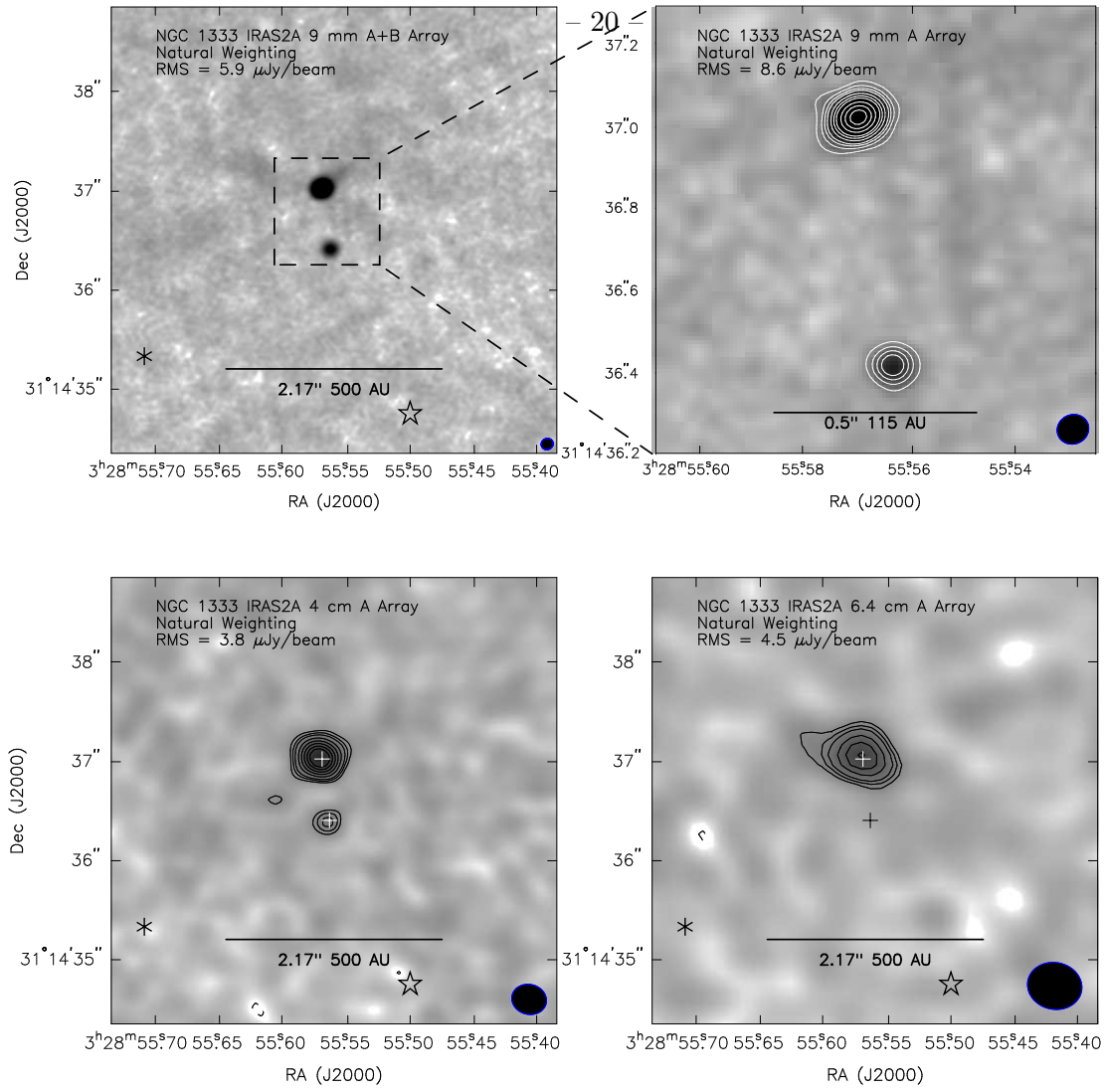

Fig. 1.— NGC 1333 IRAS2A system as observed by the VLA at 9 mm (top panels) and 4 cm and 6.4 cm (bottom panels). The top left panel shows the 9mm image from A and B configurations combined, while the zoom-in shown in the right panel is from A-array only giving the highest resolution. The two sources separated by $0\farcs621 \pm 0\farcs006$ (∼143 AU) are clearly resolved in the 9 mm images; in the A+B combined 9 mm image the brighter source (IRAS2A VLA1) has a signal-to-noise ratio (SNR) of 206 and the secondary (IRAS2A VLA2) has a SNR = 41. The sources are fainter at 4 cm, with VLA1 and VLA2 only having a SNR of 18.5 and 5.4, respectively. The source VLA1 appears resolved perpendicular to the outflow direction, possibly tracing a disk. The asterisk and star symbols mark the positions of MM2 and MM3 respectively (Codella et al. 2014a). These sources are not detected in our VLA data. The beam at 9 mm is $0\farcs12 \times 0\farcs11$ and $0\farcs08 \times 0\farcs07$ for the A+B and A-only images, respectively. The beam at 4 cm and 6.4 cm is $0\farcs35 \times 0\farcs3$ and $0\farcs55 \times 0\farcs47$, respectively. The contour levels in the A-configuration 9 mm image are [-6, 6, 9, 12, 15, 20, 30, ...] $\times \sigma$ and $\sigma = 8.6$ μJy beam^{-1}. The contour levels in the 4 cm and 6.4 cm images are [-3, 3, 4, 5, 7, 9, 11, 13, 15] $\times \sigma$ and $\sigma = 3.8$ μJy beam^{-1} and 4.5 μJy at 4 cm and 6.4 cm respectively. The crosses in the lower panels mark the positions of VLA1 and VLA2 derived from the 9 mm images in the top panels.

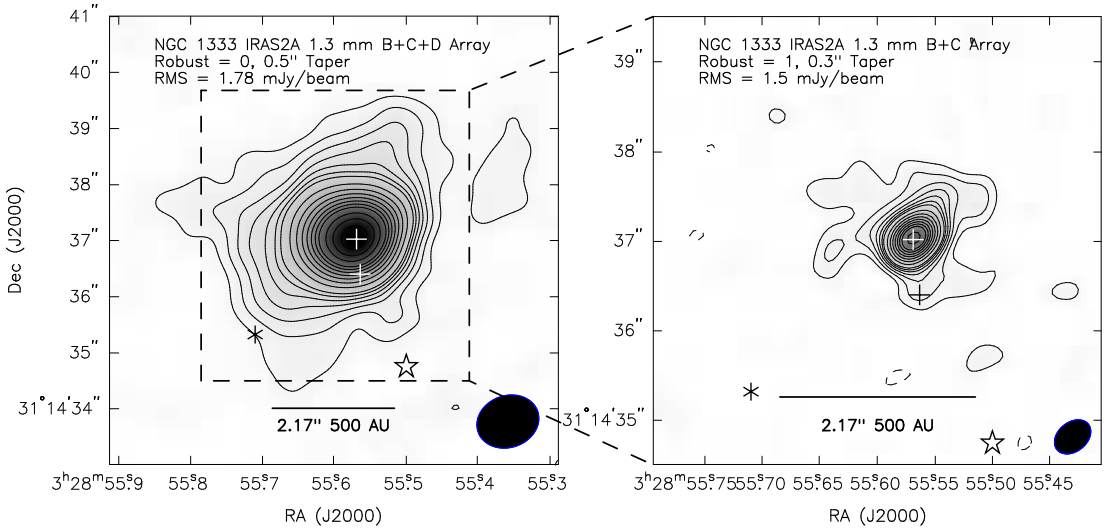
NGC 1333 IRAS2A 1.3 mm B+C+D Array
Robust = 0, 0.5" Taper
RMS = 1.78 mJy/beam
2.17" 500 AU
NGC 1333 IRAS2A 1.3 mm B+C Array
Robust = 1, 0.3" Taper
RMS = 1.5 mJy/beam
2.17" 500 AU
Dec (J2000)
RA (J2000)
RA (J2000)

Fig. 2.— NGC 1333 IRAS2A system as observed by CARMA at 1.3 mm. A lower resolution image reconstructed from a combination of B, C, and D configuration data with Robust = 0 weighting and 0.5″ tapering is shown in the left panel. A higher resolution image is shown in the right panel, combining B and C configuration data with Robust = 1 weighting and 0.3″ tapering. The crosses mark the positions of VLA1 and VLA2 derived from the 9 mm images in Figure 1. The 5σ contour in the right panel encompasses the location of VLA2. The asterisk and star symbols mark the positions of MM2 and MM3 respectively (Codella et al. 2014a). The images do not show evidence of emission at the locations of MM2 and MM3; MM2/MM3 should have been detected with $\sim 8\sigma/11.8\sigma$ in the lower resolution image and with greater SNR in the higher resolution image. The contour levels are in the left and right panels are [-3, 3, 5, 7, 9, 11, 13, 15, 20, 25, 30, 35, 40, 45, 50, 60, ...] $\times$ σ, see the respective panels for values of σ. The beam in the left panel is 1.″13 $\times$ 0.″93, and the beam in the right panel is 0.″45 $\times$ 0.″33.

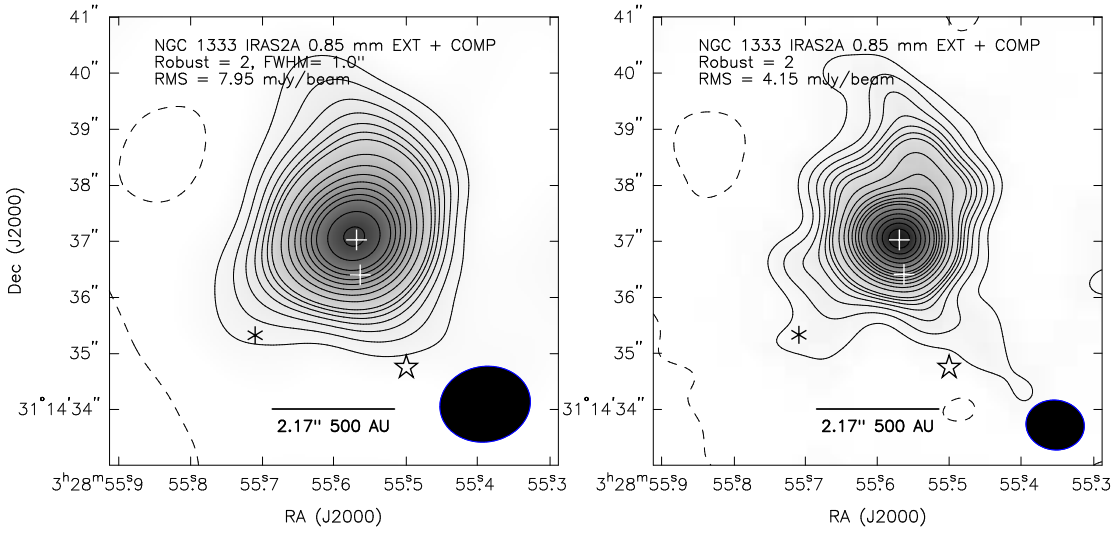

Fig. 3.— NGC 1333 IRAS2A system as observed by the SMA at 850 μm. A lower resolution image is reconstructed from a combination of Compact and Extend configuration data with Robust = 2 weighting and 1.0″ tapering is shown in the left panel. A higher resolution image is shown in the right panel Robust = 2 weighting and no tapering. The crosses mark the positions of VLA1 and VLA2 derived from the 9 mm images in Figure 1. Like Figure 2, these images also do not show evidence of discrete sources at the locations of MM2 and MM3 marked by the asterisk and star symbols respectively. MM2/MM3 have expected detection levels of $\sim 9.7\sigma/17.3\sigma$ in the higher resolution image. The contour levels are in the left and right panels are [-3, 3, 5, 7, 9, 11, 13, 15, 20, 25, 30, 35, 40, 45, 50, 60, ...] $\times \sigma$, see the respective panels for values of σ. The beam in the left panel is 1.″04 $\times$ 0.″89, and the beam in the right panel is 0.″87 $\times$ 0.″60.

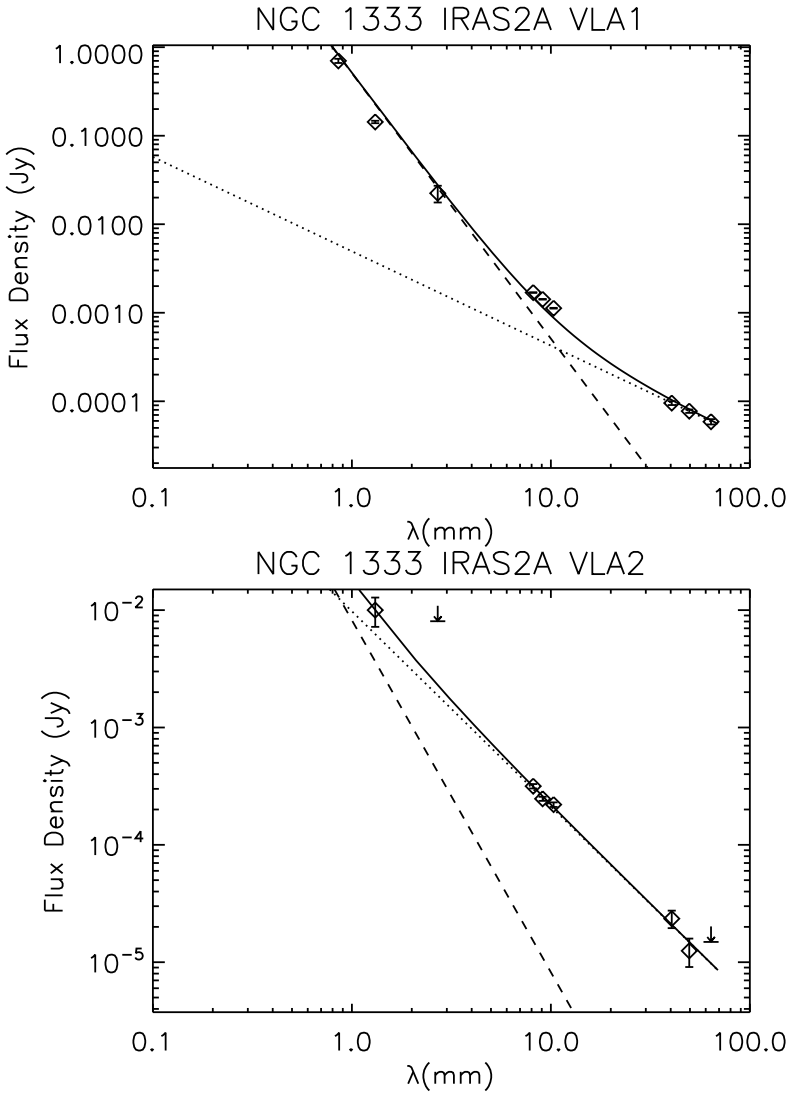

Fig. 4.— Millimeter to centimeter-wave spectra of IRAS2A VLA1 and VLA2 using the integrated intensity data from Table 1. The dotted line is a fit to the free-free slope (using only the 4 cm and 6.4 cm data for VLA1), the dashed line is a fit to the thermal dust emission slope, and the solid line is the sum of the thermal dust emission and free-free component. The 2.7 mm points for VLA1 and VLA2 are the integrated flux density and 3σ upper limits from Looney et al. (2000); the 2.7 mm flux of VLA1 is used in the fit. The 4 cm and 4.9 cm points for VLA2 are the peak flux densities rather than the integrated flux due to low signal-to-noise. For unresolved sources, like VLA2, the peak flux density is equivalent to the integrated flux.

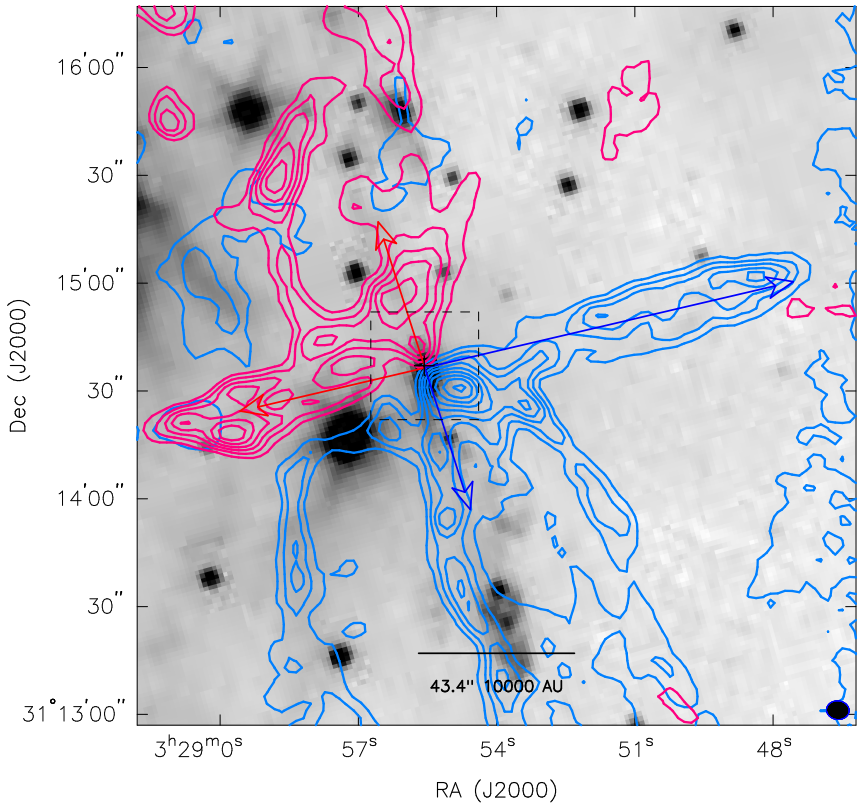

Fig. 5.— Blue-shifted and red-shifted CO ($J = 1 \rightarrow 0$) contours from Plunkett et al. (2013) overlaid on the *Spitzer* 4.5 μm image (grayscale) from Jørgensen et al. (2006). The cross marks the position of VLA1 derived from the 9 mm image in Figure 1. The CO emission traces the large-scale outflow emission associated with the IRAS2A system, showing the quadrupolar outflow from the source. The contours are [-10, 10, 20, 30, ...] $\times$ σ and σ = 0.61 K and 0.76 K for the blue and red integrated intensity maps, respectively. The beam is $6\farcs3 \times 5\farcs2$. The CO emission is integrated over 0.5 km s^{-1} to 6.5 km s^{-1} (blue contours) and 9.7 km s^{-1} to 13.5 km s^{-1} (red contours). The dashed box shows the region that viewed in CO ($J = 2 \rightarrow 1$) and ($J = 3 \rightarrow 2$) in Figure 6.

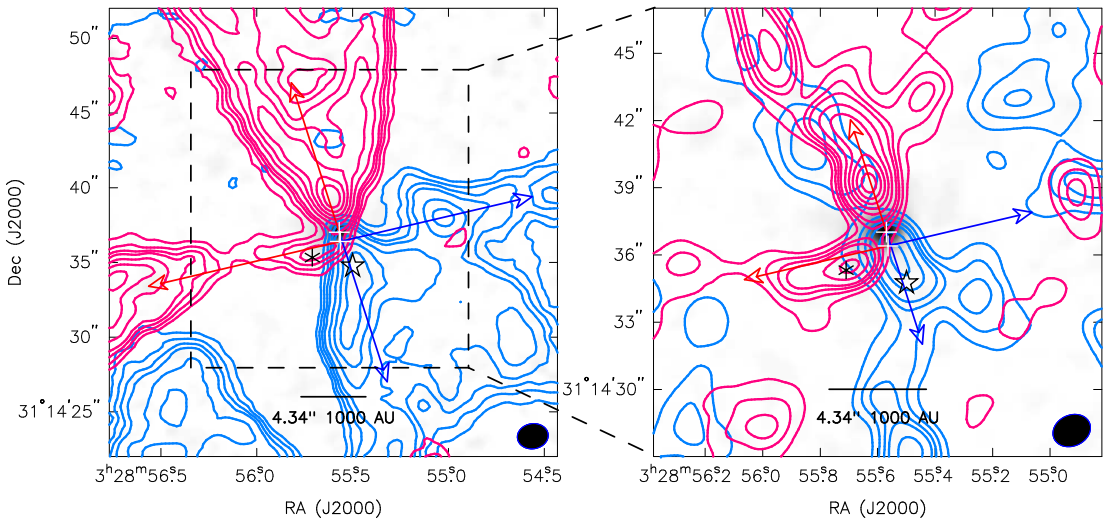

Fig. 6.— Blue-shifted and red-shifted CO ($J = 2 \rightarrow 1$) from a combination of CARMA C, D, and E-array observations with Robust = 0 weighting (left) and SMA CO ($J = 3 \rightarrow 2$) from a combination of Compact and Extended configurations with Natural weighting (right). Both outflow maps are overlaid on the CARMA 1.3 mm continuum image (grayscale). The crosses mark the positions of VLA1 and VLA2 derived from the 9 mm images in Figure 1. These higher excitation CO lines, observed at higher resolution, trace the outflowing material closer to the protostars and show that there are departures from outflow symmetry on small-scales relative to the larger scale outflow axis. The asterisk and star symbols mark the positions of MM2 and MM3, respectively, from Codella et al. (2014a). Note that MM2 lies exactly in a bright spot of CO emission traced by both transitions, and MM3 is in the blue-shifted lobe of north-south outflow. The contours are [-5, 5, 10, 15, 20, 30, ...] $\times \sigma$ for the red and blue-shifted emission in both the left and right panels. The RMS noise values are 0.81 K, 0.74 K, 0.88 K, 0.77 K for the blue and red CO ($J = 2 \rightarrow 1$) integrated intensity maps in the left panel and the blue and red CO ($J = 3 \rightarrow 2$) integrated intensity maps in the right panel, respectively. The beams are $2\farcs1 \times 1\farcs7$ in the left panel and $1\farcs7 \times 1\farcs4$ in the right panel. The CO ($J = 2 \rightarrow 1$) emission is integrated over 2.75 km s^{-1} to 5.75 km s^{-1} (blue contours) and 9.75 km s^{-1} to 12.5 km s^{-1} (red contours); the CO ($J = 3 \rightarrow 2$) emission is integrated over 1.0 km s^{-1} to 5.75 km s^{-1} (blue contours) and 9.7 km s^{-1} to 13.0 km s^{-1} (red contours).

Table 1. NGC 1333 IRAS2A Measurements

Wavelength (mm)	Array Config.	Integrated Flux Density (mJy)	Peak Flux Density (mJy/beam)	Gaussian Size ($''$)	Gaussian PA ($^\circ$)	Deconvolved Size ($''$)	Deconvolved PA ($^\circ$)	Robust	Beam ($''$)	Beam PA ($^\circ$)
VLA1										
0.85	EXT+COMP	701 ± 38	361 ± 4.6	1.15 × 0.99	87.5	0.81 × 0.74	152	-2	0.87 × 0.60	84.5
1.3	BC	143.0 ± 4.5	96.6 ± 1.5	0.56 × 0.42	134.9	0.34 × 0.26	147	1	0.45 × 0.33	-50.7
8.15	AB	1.69 ± 0.014	1.43 ± 0.0084	0.13 × 0.11	112.2	0.054 × 0.036	110.6	2	0.11 × 0.10	-66.7
8.15	A	1.73 ± 0.019	1.23 ± 0.013	0.090 × 0.071	107.9	0.055 × 0.033	109.0	2	0.07 × 0.06	-73.9
9.1	AB	1.42 ± 0.012	1.23 ± 0.0056	0.14 × 0.12	111.9	0.056 × 0.038	113.9	2	0.12 × 0.11	-69.6
9.1	A	1.44 ± 0.012	1.09 ± 0.0086	0.096 × 0.079	111.29	0.054 × 0.032	111.6	2	0.08 × 0.07	-69.3
10.3	AB	1.13 ± 0.01	0.99 ± 0.0071	0.15 × 0.13	112.0	0.058 × 0.036	117.8	2	0.13 × 0.12	-72.7
10.3	A	1.14 ± 0.014	0.91 ± 0.012	0.10 × 0.085	117.0	0.054 × 0.030	117.9	2	0.09 × 0.08	-64.7
40.5	A	0.096 ± 0.005	0.079 ± 0.0038	0.39 × 0.33	92.1	0.18 × 0.11	125	2	0.35 × 0.30	78.4
49.6	A	0.077 ± 0.004	0.066 ± 0.0034	0.47 × 0.38	76.9	0.23 × 0.11	79	2	0.41 × 0.36	75.2
63.8	A	0.0588 ± 0.004	0.054 ± 0.005	0.68 × 0.43	72.3	...	...	2	0.55 × 0.47	78.5
VLA2										
1.3[a]	BC	10.0 ± 2.8	9.7 ± 1.5	...	...	...	...	1	0.45 × 0.33	-50.7
8.15	AB	0.316 ± 0.014	0.276 ± 0.0084	0.12 × 0.11	97.6	0.049 × 0.032	39	2	0.11 × 0.10	-66.7
8.15	A	0.328 ± 0.017	0.248 ± 0.013	0.082 × 0.071	91.5	0.042 × 0.031	68	2	0.07 × 0.06	-73.9
9.1	AB	0.247 ± 0.01	0.245 ± 0.0059	0.12 × 0.11	106.1	...	...	2	0.12 × 0.11	-69.6
9.1	A	0.263 ± 0.01	0.229 ± 0.0086	0.084 × 0.076	83.8	...	...	2	0.08 × 0.07	-69.3
10.3	AB	0.220 ± 0.01	0.213 ± 0.0071	0.14 × 0.12	102.5	...	...	2	0.13 × 0.12	-72.7
10.3	A	0.221 ± 0.012	0.203 ± 0.012	0.091 × 0.082	62.4	...	...	2	0.09 × 0.08	-64.7
40.5	A	0.015 ± 0.004	0.023 ± 0.0038	...	...	...	...	2	0.35 × 0.30	78.4
49.6	A	0.008 ± 0.003	0.0125 ± 0.0034	...	...	...	...	2	0.41 × 0.36	75.2
63.8	A	<0.0015	<0.0015	...	...	...	...	2	0.55 × 0.47	78.5

Note. — All flux measurements are from Gaussian fits to the images at each wavelength, except for the peak flux densities which are directly taken from the images. We do not give uncertainties on the Gaussian fit parameters for the sake of brevity. The 1σ RMS noise for each image can be found in the uncertainty of the peak flux density. Note that the wavelengths are listed with higher precision than in the text.

[a]Due to the faintness of the source we fixed the source parameters to match the beam and we only allowed the flux to vary.

Table 2. IRAS2A Spectral Slopes

	VLA1 (fixed free-free)	VLA1 (no fixed parameters)	VLA2 (fixed thermal slope)	VLA2 ($\lambda > 7$ mm) (no fixed parameters)
Free-free Slope	1.1±0.19	0.8±0.4	1.7±0.12	1.7±0.09
F_0 (free-free)	4.9±3.5	1.5±2.5	9.8±3.2	10.2±2.0
Thermal Dust Slope	2.8±0.08	2.6±0.14	3.0	...
F_0 (dust)	379±59	316±60	8.2±1.0	...

Note. — The spectral slopes are defined by the convention $F_\lambda = F_0(\lambda/\lambda_0)^{-\alpha}$ where α is the spectral slope and λ_0 = 1 mm. The VLA2 ($\lambda > 7$ mm) values are from a single slope fit to the $\lambda > 7$ mm data, obtaining a similar slope to the fit with a fixed thermal slope.